Poly(vinyl) Alcohol-Assisted Fabrication of Magnetic Reduced Graphene Oxide Aerogels and their Adsorption Performance for Cd(II) and Pb(II)

Jiang-Bo Huo · Guoce Yu

Abstract Magnetic graphene-based aerogels have attracted intensive interest due to their unique properties. In this study, a two-step strategy was proposed to fabricate a family of magnetic reduced graphene oxide aerogels (abbreviated as rGO/Fx, x = 1, 2 and 3) as adsorbents for removing heavy metals from water. The hydrogen bonds between poly(vinyl) alcohol (PVA) and rGO maintained the integrity of the rGO/Fx structures evidenced by FT-IR and Raman spectra. The rGO/Fx showed a unique structure with nanoparticles/nanoplates embedded on rGO sheets by SEM observation. The rGO/Fx consisted of PVA, rGO and Fe-based species (Fe_3O_4, Fe^0 and FeOOH) identified by PXRD, TGA and XPS analysis. The impressive magnetic property of rGO/Fx can be easily tuned by the mass ratio of Fe/GO. The saturation magnetizations were 0.50, 0.72, and 9.59 emu/g for rGO/F1, rGO/F2 and rGO/F3, respectively. The capacity of rGO/F1 was calculated to be 21.84 and 16.10 mg/g for Cd^{2+} and Pb^{2+}, respectively. This study may contribute a novel synthesis method of magnetic graphene aerogels by using polymers and metals, and offer an alternative adsorbent for removing heavy metals.

J.-B. Huo · G. Yu (✉)
Laboratory of Environmental Technology, INET, Tsinghua University, Beijing 100084, China
e-mail: yugc@tsinghua.edu.cn

1 Introduction

Graphene, exfoliated from natural graphite, is a two-dimensional (2D) carbon layer material, which has attracted extensive interest in the fields of chemistry and material science, due to its unique structure, large specific surface area and excellent mechanical property (Cong et al., 2014; Mao et al., 2015). Though graphene is theoretically a superior adsorbent, it cannot practically achieve this purpose. The main reason is that graphene nanosheets are usually prone to restacking up driven by weak van der Waals attractions among individual layers, severely reducing its specific surface area and restricting its application (Jiang & Fan, 2014; Perreault et al., 2015).

In this regard, three-dimensional graphene aerogels (3D GA) assembled from 2D sheets have drawn considerable attention (Upadhyay et al., 2014). In comparison with the 2D structure, 3D GA contain diverse hierarchical pores including micro-, meso- and macropores, in which the texture of the micro- and mesoporosity can generate a large specific surface area and the texture of the macroporosity can guarantee easy mass transfer to internal surfaces (Mao et al., 2018; Shen et al., 2015). This feature is greatly beneficial to the improvement of adsorption performance. Notably, the macroscopic monolith morphology makes 3D GA convenient for manipulation and collection in application (Kemp et al., 2013).

Based on these distinct properties, 3D GA has exhibited remarkable advantages (Qiu et al., 2018). A number of synthesis strategies for 3D GA have been reported, such as self-assembly, template-assisted preparation and direct deposition. Among these, the self-assembly method can afford a convenient and scalable process to fabricate graphene aerogels with excellent thermal stability (Chen & Yan, 2011; Cong et al., 2014; Xu et al., 2010a, 2010b). Many materials, such as DNA, organic molecules, metal ions and polymers, have already been used as cross-linkers for the self-assembly of GO sheets via covalent bonding, electrostatic interaction, and hydrogen bonding (Cao et al., 2014; Xu et al., 2010a, 2010b).

To expand the potential application of 3D GA, numerous efforts have been made for the fabrication of the 3D GA composites with designable and controllable structures. For instance, graphene was deposited on diverse template surfaces including spongy Ni foam, polystyrene spheres, silica spheres, and cellulose, and then the corresponding composites were easily garnered (Luo & Zhi, 2015). Moreover, the incorporation of 3D GA with other nanostructures (e.g. NPs, nanorods, nanotubes, and nanosheets) is deemed as an efficient method for the fabrication of new composites (Cong et al., 2014). Among them, magnetic composites have been highlighted due to their unique magnetic property. These composites integrate the porous structure of 3D GA and the property of magnetic nanoparticles (Sahraei et al., 2017; Wu et al., 2019).

Magnetic aerogels can be prepared by several methods. For instance, ferrous ions can be used as reductants for GO self-assembly, and their products would be decorated on the resultant 3D GA (Cong et al., 2012). A polymer-template method was also proposed for the synthesis of magnetic aerogels, and this method can enhance nanostructures of the aerogel (Zhuang et al., 2019). Recently, another strategy combining filler-loaded networks with vacuum freeze-drying was used to fabricate magnetic aerogels. This method can endow the resultant aerogels with strong superparamagnetic behavior (Arabkhani & Asfaram, 2020).

However, the aerogels usually suffer from unsatisfactory structural stability, which has limited their application. Polymers or metal ions can induce crosslinking of GO, and reinforce the structure of aerogels by different mechanisms. Presumably, structural stability of aerogels may tend to be enhanced by combining polymers and metal ions. However, the study about fabrication of magnetic graphene-based aerogels by a simple method is still scarce.

In this study, we proposed a combination strategy for preparation of magnetic aerogels, which combined the template effect of poly(vinyl) alcohol (PVA) and the modification functionality of iron species. The role of PVA was investigated in the formation of rGO/Fx. The iron species in the resultant aerogels were identified based on characterization technologies. The tuning mechanism of magnetic property of rGO/Fx was also studied. Taking Cd^{2+}/Pb^{2+} as model pollutants, the adsorption performance of rGO/Fx was primarily estimated. This study aims to provide a novel synthesis concept of magnetic aerogels by using polymers and metal ions.

2 Experimental Section

2.1 Materials and Reagents

Graphene oxide (GO) suspension (10 mg/mL), poly(vinyl) alcohol (PVA, $M_w \sim 145,000$), $FeCl_3 \cdot 6H_2O$, $Pb(NO_3)_2$, $NaBH_4$, and $Cd(NO_3)_2 \cdot 4H_2O$ were provided by Sinopharm Chemical Reagent Co., Ltd. (Shanghai, China). All chemicals in this study were of analytical grade and used directly without any further purification. The cadmium and lead standard solutions (1000 mg/L) were purchased from General Research Institute for Nonferrous Metals (Beijing, China). Pb(II) and Cd(II) stock solutions were prepared by dissolving corresponding nitrate salts in ultrapure water, respectively.

2.2 Synthesis of rGO/Fx

A two-step strategy was applied to fabricate a family of magnetic poly(vinyl) alcohol/graphene oxide (labeled as: rGO/Fx, x = 1, 2, 3).

Typically, a certain amount of Fe^{3+} and PVA (16 g/L) were dissolved in hot ultrapure water with vigorously stirring for 2 h, preparing three concentrations of Fe^{3+} by varying the mass of $FeCl_3 \cdot 6H_2O$ (solution 1: 0.013 mol/L, solution 2: 0.026 mol/L, solution 3: 0.052 mol/L). 8 mg/mL GO suspension was prepared by diluting GO stock solution. Then, the as-prepared GO suspension was evenly divided into dozens of aliquots in some small beakers (2.5 mL of suspension in each beaker). In each beaker, 0.625 mL of mixing solution containing Fe^{3+} and PVA was added dropwise into GO suspension and stirred rapidly to accelerate gelation. Several seconds later, the hydrogel of PVA/GO/Fe^{3+} was thus formed. After freeze drying, the PVA/GO/Fe^{3+}

aerogel was naturally obtained. Adding the solutions 1, 2, and 3, we could prepare a family of aerogels, namely, PVA/GO/Fe^{3+}-y, y = 1, 2, 3. For comparison, two control experiments were also conducted as follows: one was without PVA and the other was no addition of Fe^{3+}. The corresponding aerogels were labelled as GO/Fe^{3+} and PVA/GO.

In the reducing process, the experiment groups and control groups were impregnated in $NaBH_4$ solution (0.1 mol/L) and a redox reaction was initiated at room temperature under the nitrogen atmosphere, resulting in the conversion of Fe^{3+} and GO. After 2 h reaction, the as-synthesized hydrogels were rinsed for several times with ultrapure water until pH of eluting solutions became neutral. These hydrogels were dried again by lyophilization to yield rGO/Fx, PVA/rGO and rGO/Fe.

2.3 Characterization of rGO/Fx

The morphology and surface element species of the as-prepared rGO/Fx series were characterized via a field emission scanning electron microscopy (FESEM) combined with an energy dispersive X-ray (EDX) system (Hitachi SU-8010, Japan). The crystalline phases of rGO/Fx series were examined by an X′Pert PRO diffractor (PANalytical, Holland, Cu Kα, λ = 0.15406 nm) under the condition of 40 kV and 40 mA. Fourier transforming infrared spectra (FT-IR) were recorded on a total reflection infrared spectrometer (Thermo Fisher Scientific, Nicolet-6700, USA). Raman spectra were obtained via a Raman spectrometer (Horiba HR-800, France, λ = 532 nm). The specific surface areas and pore distributions of rGO/Fx series were calculated from the nitrogen adsorption–desorption isotherms, determined on an automatic chemical adsorption instrument (Quantachrome Autosorb-1, USA). X-ray photoelectron spectra (XPS) of rGO/Fx series were examined in a PHI 5000C ESCA system (PHI, USA). The stability of rGO/Fx series was measured on a thermogravimetric analyzer (TGA, PerkinElmer, USA) from 25 ℃ to 800 ℃ at a rate of 10 ℃/min. The magnetic intensity of rGO/Fx series was determined under the condition of ± 20,000 Oe at 300 K by Vibrating Sample Magnetometer (VSM, MPMS-3, USA).

2.4 Adsorption Performance

The adsorption tests were conducted in conical flasks containing 100 mL of pollutant solution (Cd^{2+}/Pb^{2+}) and 50 mg of rGO/Fx, which were placed in a shaker and continuously stirred. At predetermined time intervals (~ 360 min), an aliquot of supernatant was taken from the containers by using 1 mL pipette, and then filtered with syringes equipped with polytetrafluoroethylene filters (0.22 μm of pore diameter). The collected filtrate was stored for subsequent analysis.

Ionic samples were measured by polarized Zeeman Atomic Absorption Spectrophotometer ZA3000 Series (AAS, Hitachi, Japan). In this study, all adsorption experiments were carried out in duplicate and the corresponding average values were reported. The adsorption amounts (q) were calculated from the following Eq. 1, and Eqs. 2 and 3 are mathematical expressions of the pseudo first-order model (PFO) and the pseudo second-order model (PSO) (Dai et al., 2019; Guo & Wang, 2019; Yu et al., 2017):

$$q_t = \frac{(C_0 - C_t) \times V}{m} \tag{1}$$

$$q_t = q_e(1 - e^{-k_1 t}) \tag{2}$$

$$q_t = \frac{k_2 q_e^2}{1 + k_2 q_e t} t \tag{3}$$

where C_0 and C_t (mg/L) are initial concentration and instant concentration (at time t) of Cd^{2+} and Pb^{2+} in the solution, respectively. V (mL) represents the solution volume, and m (mg) is the mass of rGO/Fx. q_t and q_e (mg/g) are the instant and equilibrium adsorption amounts, respectively. k_1 (min^{-1}) and k_2 (g mg^{-1} min^{-1}) are the kinetic constants of PFO and PSO, respectively.

3 Results and Discussion

3.1 The Role of PVA in the Fabrication of rGO/Fx

During the synthesis process, an interesting phenomenon can be found that when PVA participated in the reaction, the rGO/Fx morphology was generally retained after even undergoing a redox reaction, otherwise it would be highly loose (control group: rGO/Fe). Considering this fact, it can be inferred that PVA may act as an important role in maintaining the structure intactness (Zakaria & Kamarudin, 2021; Zhang et al., 2018). In the first step, PVA and Fe^{3+} played a synergistic role in the gelation due to the strong hydrogen bonds and electrostatic attraction (Mohammadian et al., 2019).

**Scheme 1** The role of PVA in the synthesis of rGO/Fx
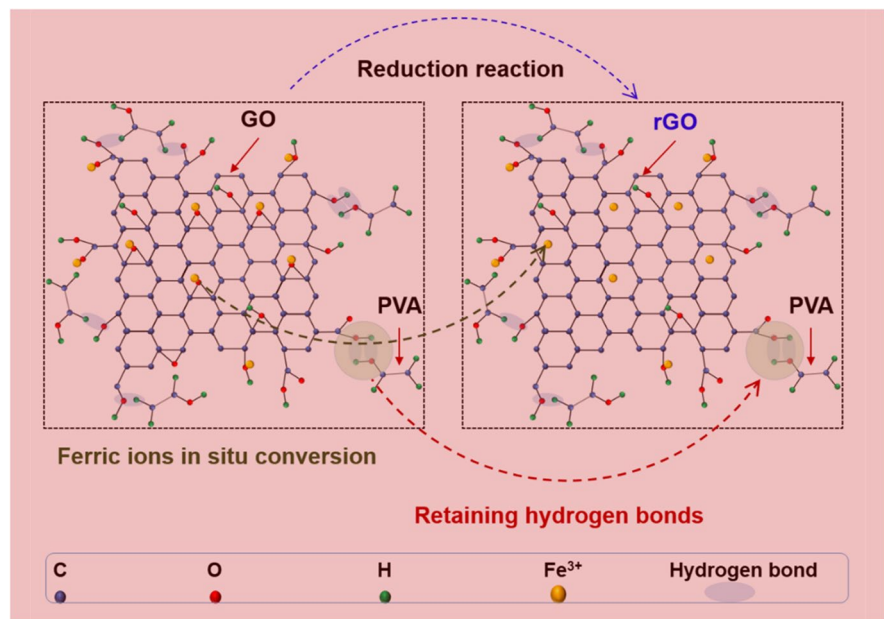
As displayed in the Scheme 1, there were three main changes when PVA/GO/Fe^{3+} reacted with $NaBH_4$. Firstly, GO was converted into reduced GO (rGO), in other words, these epoxy groups on the GO sheets were reduced (De Silva et al., 2017). Secondly, excess $NaBH_4$ would further reduce in situ ferric ions into Fe_3O_4 or Fe^0, even other iron-based species (Zou et al., 2016). Lastly, accompanying by the transformation of GO into rGO, a few hydrogen bonds were broken due to the disappearance of epoxy groups, while most hydrogen bonds, built among hydroxyl groups of PVA and hydroxyl/carboxyl groups on the basal plane of GO or rGO, were maintained. These hydrogen bonds could play against the dispersion of adjacent GO sheets, thus reserving an intact aerogel. Therefore, PVA is deemed as a necessary constituent to enhance the structural stability.

3.2 Morphology and Structure of rGO/Fx

The morphology of rGO/F1, rGO/F2 and rGO/F3 is displayed in Fig. 1. rGO/F1 possessed a stacking structure made up of sheets (Fig. 1a-b), as a result of the self-assembly of rGO sheets when redox reaction occurred. Only a small portion of iron-based species were attached to the sheets surface. No other species were recognized on the smooth surface from the magnification image (Fig. 1c). The porous crosslinking structure densely decorated by small nanoparticles

was discovered from the images of rGO/F2 and rGO/F3 (Fig. 1d-e). These nanoparticles can be ascribable to the Fe-based species produced in the redox reaction.

In comparison with rGO/F1, the micromorphology of rGO/F2 and rGO/F3 exhibited a relatively compact but hierarchical structure. This may be because the Fe^{3+} intercalator imposed a strong attraction on the sheet structure when the mass ratio of Fe/GO increased. Although an increasement of Fe amount inevitably cause a low tenacity originated from the salting-out effect, PVA can restrain the detachment of rGO sheets via strong hydrogen bonds and molecular viscosity property (Dai et al., 2018; Yi et al., 2018). Driven by the resultant action, a hierarchical porous but dense structure of rGO/Fx (x=2, 3) was eventually formed, and such a structure may show diverse features in terms of SAA and pore size distributions. Comparing Figs. 1f and i, we found another interesting phenomenon that the Fe-based species in rGO/F2 were mostly composed of nano-scale plates, while rGO/F3 consisted of a mixture of nanoplates and nanoparticles. This suggested that the Fe-based species were different when the mass ratios of Fe/GO were different. In other words, the structure and property of the as-synthesized aerogels can be tunable by adjustment of Fe/GO ratio. Except rGO/F1, rGO/F2 and rGO/F3 possessed a unique structure of nanoparticles- and nanoplates-on-sheets (Vafakhah et al., 2019; Wu et al., 2019).
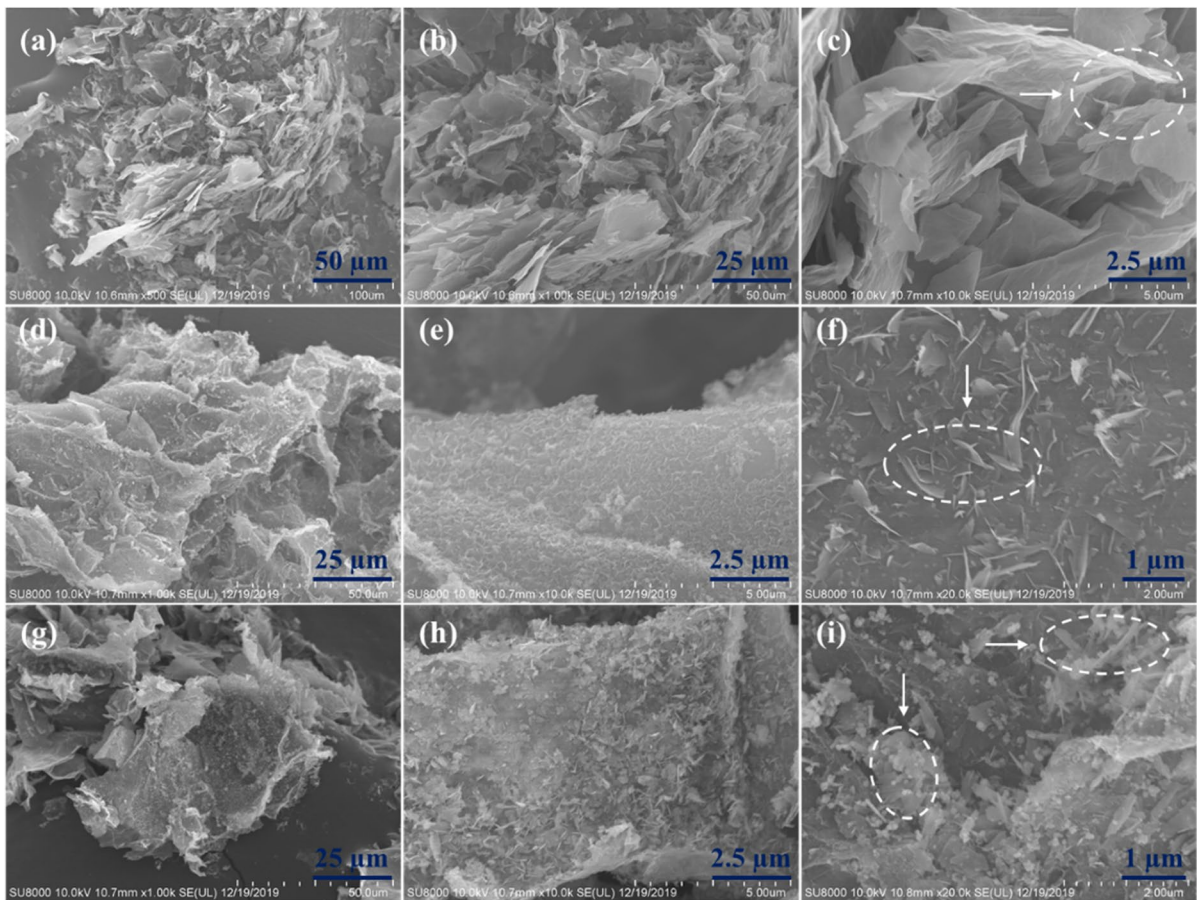
Fig. 1 FESEM images of rGO/F1 (**a-c**), rGO/F2 (**d-f**) and rGO/F3 (**g-i**)

The elemental compositions of rGO/Fx were examined by SEM–EDX. As shown in Fig. 2, rGO/Fx series were basically made of carbon, oxygen and iron elements. The iron contents were approximately 2.86%, 4.35%, and 11.63% for rGO/F1, rGO/F2, and rGO/F3, respectively. Iron contents showed an increment increasing at elevated mass ratios of Fe/GO. In view of the morphological difference, it is speculated that the composition and the property of the rGO/Fx series would be different.

PXRD spectra of the rGO/Fx series are depicted in Fig. 3a. As is known, the characteristic peak of GO was generally located at $2\theta = {\sim}11°$. After reduction of GO, a new peak appeared at $2\theta = 26.5°$ and this could confirm the conversion of GO into rGO (Liang et al., 2018). Moreover, a broad peak centered at $2\theta = 20.5°$, which is assignable to the typical peak of PVA (Dai et al., 2018). Peaks located at $2\theta = 13.5°/23.5°$ were in line with those of orthorhombic iron hydroxide oxide (FeOOH, PDF No. 01–070-0714). The other two peaks at $2\theta = 35.8°$ and 43.9° were consistent with those of orthorhombic Fe_3O_4 (PDF No. 01–075-1609) and cubic Fe^0 (PDF No. 01–001-1252), respectively (Chen et al., 2019; Tang & Wang, 2018a, 2018b; Yao et al., 2019a, 2019b). By analysis above, the Fe-based species of rGO/F1 were mostly FeOOH, while those of rGO/F2 and rGO/F3 contained FeOOH, Fe_3O_4 and Fe^0. Moreover, rGO/F2 and rGO/F3 differed in the relative contents of Fe-based species.

FT-IR spectra of PVA/GO (as a reference) and rGO/Fx series are shown in Fig. 3b. A small peak at 611 cm^{-1} was probably assigned to the vibration of Fe–O (Feng et al., 2017; Yao et al., 2019a, 2019b), implying the existence of FeOOH and Fe_3O_4 in the rGO/Fx series. This is consistent with the PXRD
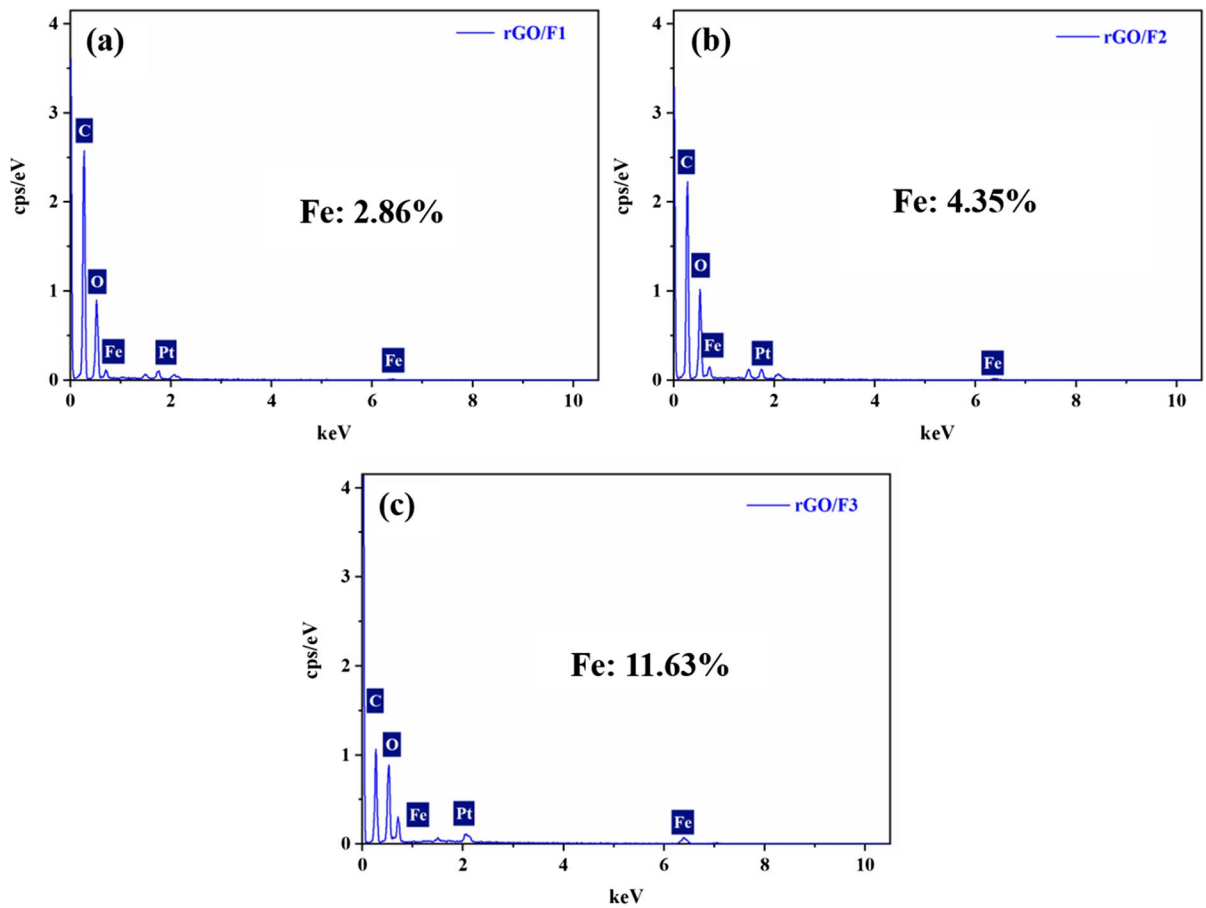
Fig. 2 SEM–EDX spectra of rGO/F1 (**a**), rGO/F2 (**b**) and rGO/F3 (**c**)
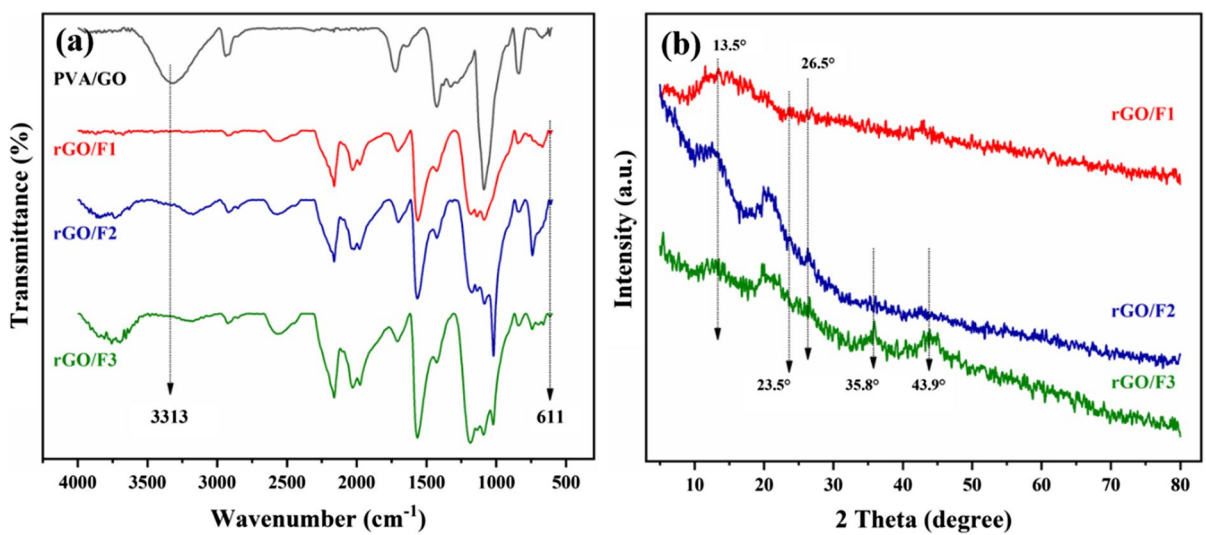

Fig. 3 PXRD patterns (**a**) and FT-IR spectra (**b**) of rGO/F1, rGO/F2 and rGO/F3

analysis. Comparing to the reference spectrum (PVA/GO), an obvious difference can be observed in those spectra of rGO/Fx series, i.e., the peak of hydroxyl groups (or hydrogen bonds) shifted to a short-wave direction along with an intensity fading. This phenomenon was probably related to the partial removal of hydrogen bonds, originated from the reduction of epoxy groups on GO (Fu, et al., 2018). However, the residual hydrogen bonds were enough to preserve the mechanical property of the resultant rGO/Fx series. Without PVA participation, a monolith structure would not be well preserved. The facts suggested that PVA played an essential role in the synthesis of the rGO/Fx series.

In general, the value of I_D/I_G reflects the defect degree of carbon-based materials, and also represents the mechanical stability of the materials to some extent (Xia et al., 2017; Xiao et al., 2013). To clearly identify the roles of PVA and ferric ions, Raman spectra of the control groups (without addition of PVA or Fe^{3+}) and experiment groups were examined before and after reduction, as shown in Fig. 4. The value of I_D/I_G of GO/Fe^{3+} was 1.00, while it increased to 1.25 after reduction (Fig. 4a), which suggested that ferric ions raised the defect degree in the structure. As for PVA/GO, the value of I_D/I_G remained almost unchanged (from 0.96 to 0.93, in Fig. 4b). This indicated that PVA had a slight effect on the defect structure. Screening the spectra of rGO/Fx series (Fig. 4c-4e), we found that all these values increased, but the increment showed a decline trend as the mass ratio of Fe/GO increased. This finding can be explained by these ferric ions can create structural defects or cause the distortion deformation, while this ability
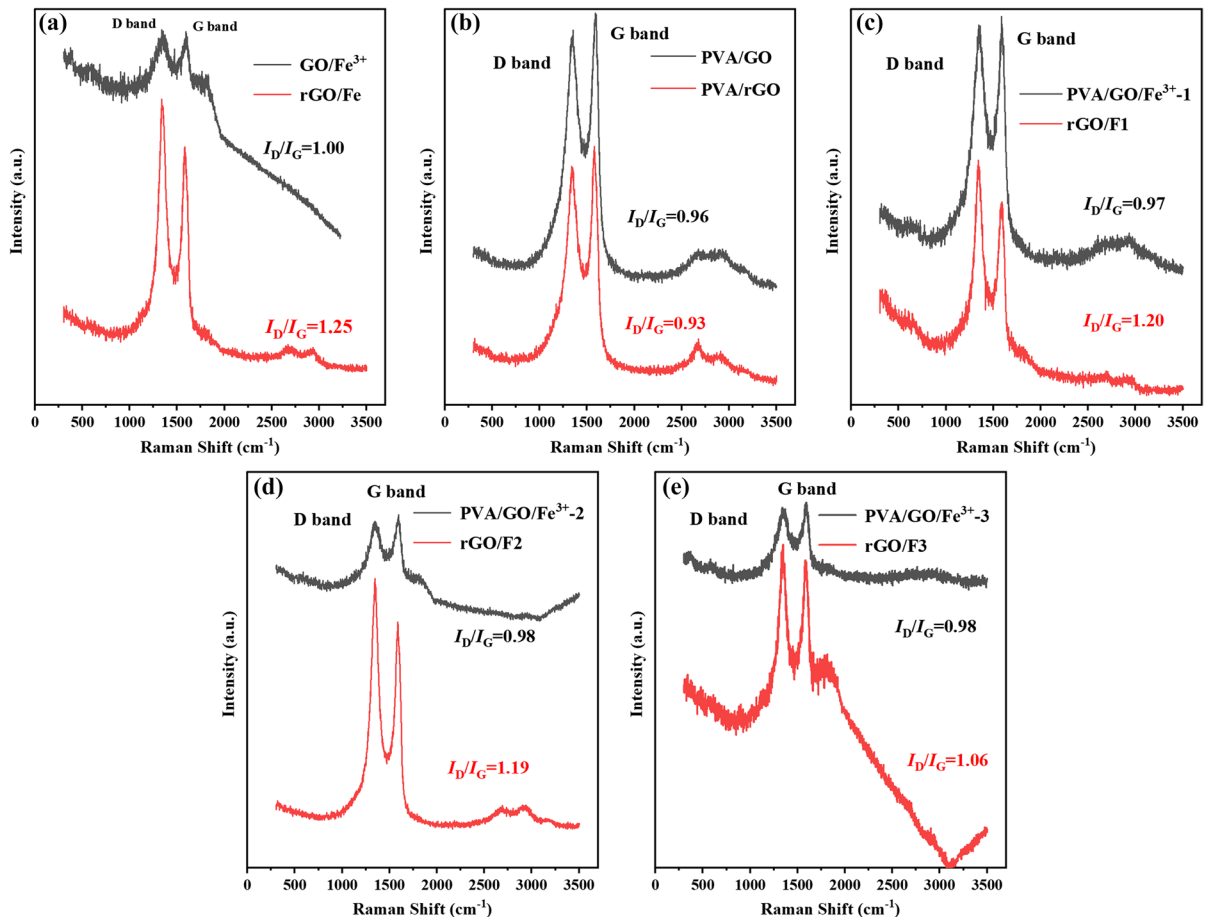

Fig. 4 Raman spectra of GO/Fe^{3+} and rGO/Fe (**a**), PVA/GO and PVA/rGO (**b**), PVA/GO/Fe^{3+}-1 and rGO/F1 (**c**), PVA/GO/Fe^{3+}-2 and rGO/F1 (**d**), PVA/GO/Fe.$^{3+}$-3 and rGO/F1(**e**)

is probably different for different Fe-based species. Overall, the morphology of rGO/Fx series were prone to more complexity after a redox reaction, as observed from the SEM images. The structural defect is usually conducive to interfacial processes such as adsorption or catalysis.

The nitrogen adsorption–desorption isotherms and the corresponding pore size distribution curves of rGO/Fx series are presented in Fig. 5. The BET specific surface areas (SSA) are 23.9, 33.6, and 29.1 m^2/g, and the average pore diameter (APD) are 13.3, 18.0, and 17.3 nm for rGO/F1, rGO/F2 and rGO/F3, respectively. Apparently, these data reflected the mesoporous nature (H3 hysteresis loop observed in the isotherms) of rGO/Fx series, and this mesoporous structure is favored for adsorption and catalysis process (Li et al., 2018a, 2018b). The SSA and APD showed a similar trend: they increased firstly followed by

a decline as the mass ratio of Fe/GO increased. Taking analysis of SEM and PXRD into account, we speculated the encapsulation of FeOOH nanoplates enlarged the SSA, but when plenty of Fe_3O_4 nanoparticles were generated in rGO/F3 structure, the agglomeration effect inversely reduced the SSA. Additionally, the SSA contribution of different Fe-based species may be different. Overall, both larger SSA and decoration by Fe-based species would play positive roles in the adsorption and catalysis process.

TG was determined in the temperature range of 40 °C—800 °C under air atmosphere, and the curves are shown in Fig. 6a. Below 200 °C, 8.2% weight loss in rGO/Fx series generally were assigned to the evaporation of water molecules. In the range of 200 – 400 °C, 36.3% weight loss for rGO/F1 and rGO/F2, and 26.3% weight loss for rGO/F3 were mostly caused by the decomposition of oxygen-containing
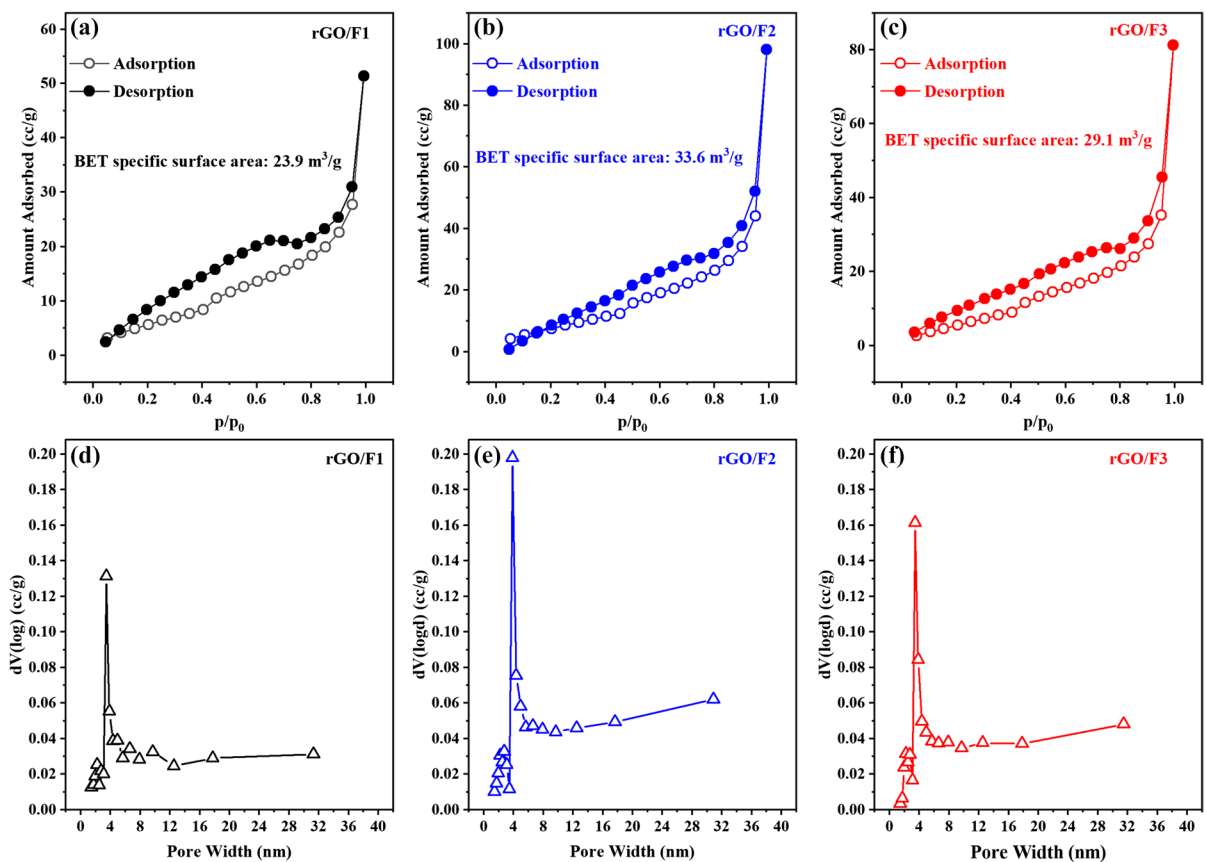
Fig. 5 The nitrogen adsorption–desorption isotherms of rGO/F1 (**a**), rGO/F2 (**b**) and rGO/F3 (**c**) and the pore size distributions of rGO/F1 (**d**), rGO/F2 (**e**) and rGO/F3 (**f**)
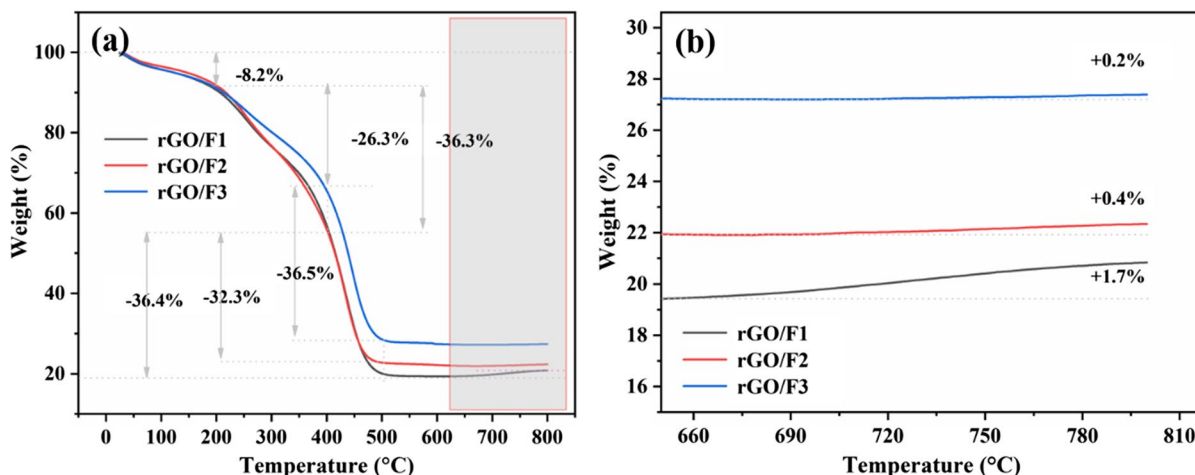
Fig. 6 TG curves (**a**) and local magnification curves (**b**) of rGO/F1, rGO/F2 and rGO/F3

groups of GO and PVA (Mohammadian et al., 2019). In the range of 400 ℃—500 ℃, 36.4%, 32.3%, and 36.5% weight loss for rGO/F1, rGO/F2, and rGO/F3, respectively, can ascribe to the decomposition of rGO (Zhuang et al., 2019). Above 600 ℃, a weight increasing trend can be found in the rGO/Fx, as presented in Fig. 6b. The weight increments for rGO/F1, rGO/F2, and rGO/F3 were 1.7%, 0.4%, and 0.2%, respectively. This abnormal phenomenon may be generated from the conversion of Fe_3O_4 into Fe_2O_3. For rGO/Fx series, the end-products consisted of Fe_2O_3, a stable phase. The basic components of rGO/Fx can be approximately obtained, as listed in Table 1.

The magnetic hysteresis loops of rGO/Fx series are shown in Fig. 7. The saturation magnetizations were 0.498, 0.716, and 9.592 emu/g for rGO/F1, rGO/F2 and rGO/F3, respectively. rGO/F1 and rGO/F2 exhibited weak magnetic properties while rGO/F3 had a strong property. This phenomenon can be explained by different Fe contents and different magnetic species contents. Moreover, an obvious loop can be seen

**Table 1** The components of rGO/Fx series calculated from TGA results (% weight)

rGO/Fx	PVA	rGO	Fe_3O_4, Fe^0 and FeOOH
rGO/F1	36.3	36.4	19.1
rGO/F2	36.3	32.3	23.2
rGO/F3	26.3	36.5	29.0

from the rGO/F3 curve, suggesting its ferromagnetism nature (Tang & Wang, 2019). Seeing the inset of Fig. 7, rGO/Fx series can be adsorbed to a magnet surface (the inset of Fig. 7). The rGO/Fx series with magnetic properties make them promising in the adsorption/catalysis process.

From XPS survey spectra of rGO/Fx series (Fig. 8a), three peaks at 284.8, 532.5, and 711.3 eV can be ascribed to typical peaks of C 1 s, O 1 s, and Fe 2p, respectively (Tang & Wang, 2019). This suggested that rGO/Fx series mainly consisted of C, O and Fe elements, which was in accordance with the SEM–EDX analysis. Figure 8b and d illustrate the high-resolution spectra of Fe 2p from Gaussian curve
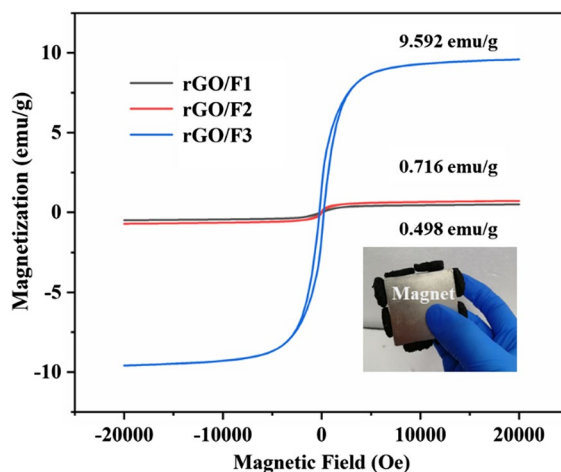

Fig. 7 Magnetization curves of rGO/F1, rGO/F2 and rGO/F3
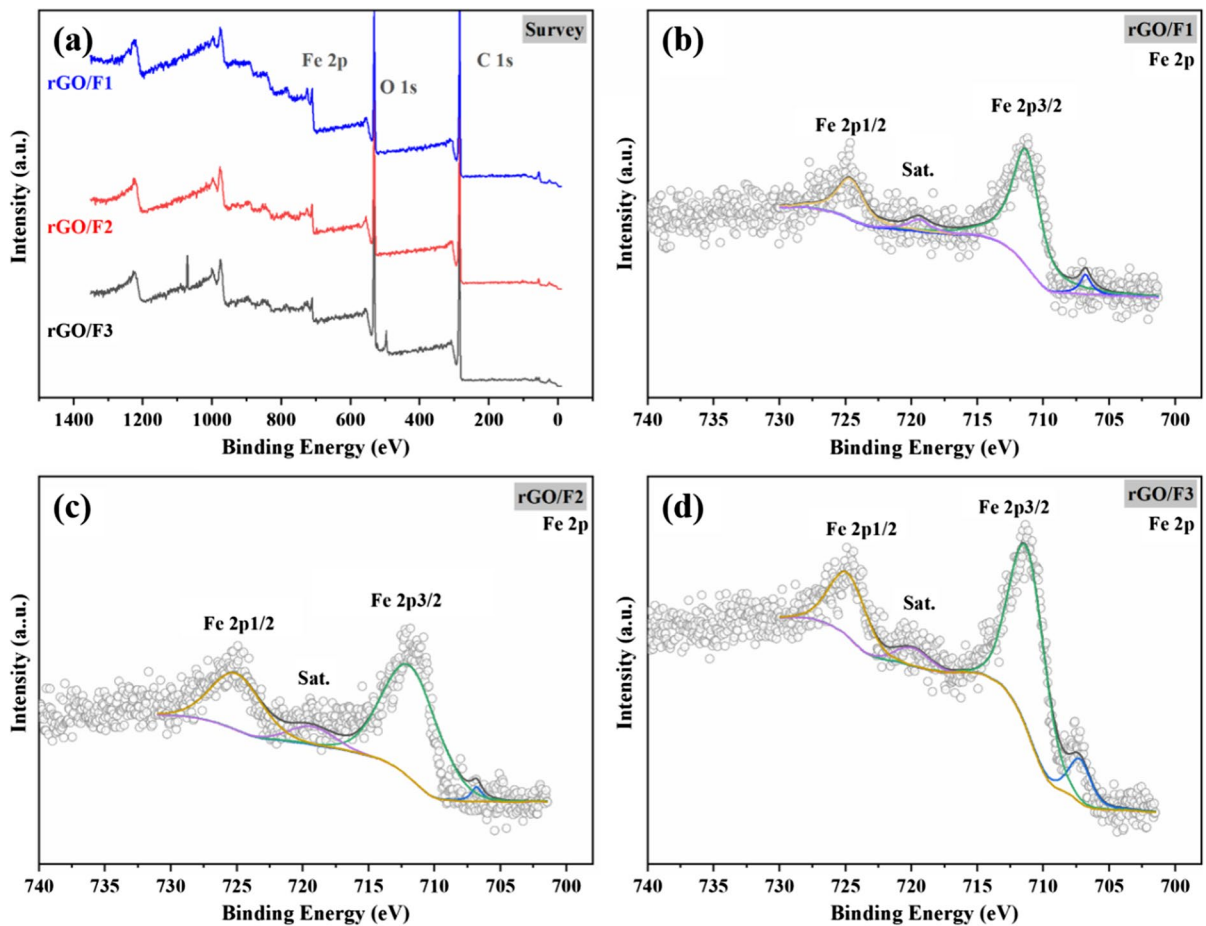
Fig. 8 Full survey XPS spectra of rGO/Fx (**a**), Fe 2p XPS spectra of rGO/F1 (**b**), Fe 2p XPS spectra of rGO/F2 (**c**) and Fe 2p XPS spectra of rGO/F3 (**d**)

fitting. Two intense peaks at 725.0 and 711.8 eV were ascribed to the representative peaks of Fe $2p_{1/2}$ and Fe $2p_{3/2}$, and the other two small peaks at 719.3 and 706.8 eV were typical satellite peaks of Fe^{3+} and Fe^0, respectively (Shao et al., 2019; Tang & Wang, 2018a, 2018b). Moreover, the intensity of these satellite peaks gradually increased when the mass ratio of Fe/GO increased. These findings suggested that the relative content of Fe_3O_4 and Fe^0 increased (Li et al., 2018a, 2018b). Thus, the magnetism intensity of rGO/Fx became strong as the mass ratio of Fe/GO increased.

Peaks of C 1 s and O 1 s can be deconvoluted into several typical peaks, as shown in Fig. 9. For O 1 s, it was divided into three subspecies including HO-H (located at ca. 536.1 eV), O = C (located at ~ 532.5 eV) and O-Fe (located at ~ 530.5 eV).

These results confirmed that there were hydroxyl groups, carboxyl groups and iron oxide or iron hydroxide in the rGO/Fx series (Wu et al., 2019). The hydroxyl groups were likely related to PVA, water and rGO whereas the carboxyl groups were mostly associated with rGO. Hydroxyl groups were occupied due to hydrogen bond interaction, and carboxyl groups could be responsible for Fe-based species attachment or as free groups for cation capture. The species contents are provided in Table 2. The relative contents of carboxyl groups accounted for approximately 85% and the relative contents of hydroxyl groups and metal–oxygen bonds only accounted for ~ 5% and ~ 10%, respectively. The contents of metal–oxygen bonds in rGO/F3 (~ 14.56%) were mostly linked to the high mass ratio of Fe/GO.
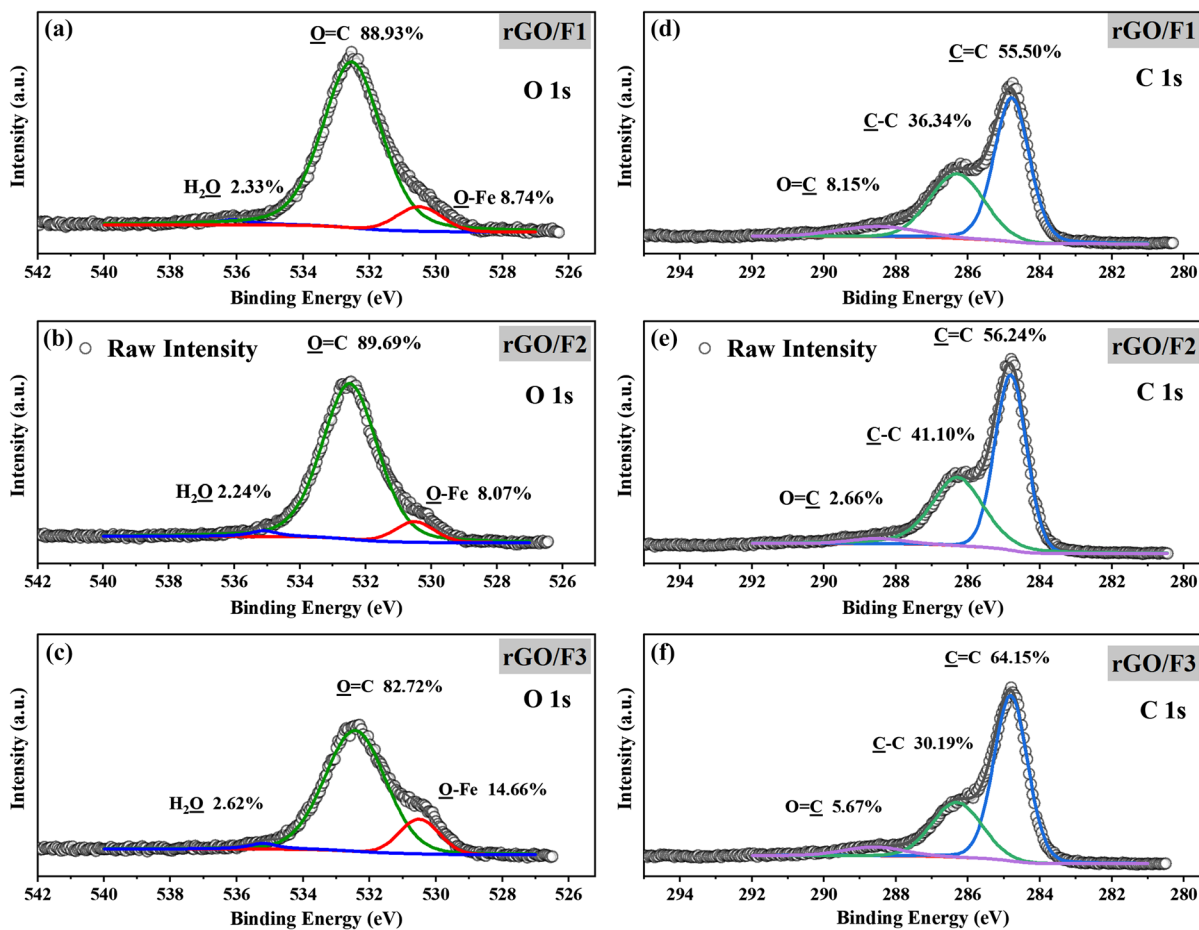
Fig. 9 O 1 s (**a**, **b**, **c**) and C 1 s (**d**, **e**, **f**) XPS spectra of rGO/Fx

Likewise, the C 1 s species were deconvoluted into three main subspecies C=O (~288.5 eV), C–C (~286.3 eV) and C=C (~284.8 eV) (Shao et al., 2019). The C=O (carboxyl groups) and C=C (sp2 hybridization) were in main connection with rGO while the C–C bonds (sp3 hybridization) were deemed as evidence of existence of PVA. As listed in Table 2, the contents of C=C are the highest (~60%), and those of C–C and C=O accounted for ~35% and ~5%, although their contents showed a slight fluctuation with the mass ratio of Fe/GO.

3.3 Adsorption of Cd(II)/Pb(II) on rGO/Fx

As shown in Fig. 10a and c, the instant concentrations (C_t) of Cd^{2+} and Pb^{2+} decreased rapidly when the contact time increased. It seems that the adsorption

performance was inversely proportional to the mass ratio of Fe/GO. The rGO/F1 can adsorb Cd^{2+} and Pb^{2+} with a better activity to a low residual concentration (0.52 and 3.45 mg/L for Cd^{2+} and Pb^{2+},

Table 2 Relative contents of oxygen and carbon element species of rGO/F1, rGO/F2 and rGO/F3 in high resolution XPS spectra (%)

Carbon species	rGO/F1	rGO/F2	rGO/F3
C=C	55.50	56.24	64.15
C–C	36.34	41.10	30.19
C=O	8.15	2.66	5.67
Oxygen species	rGO/F1	rGO/F2	rGO/F3
O-Fe	8.74	8.97	14.66
O=C	88.93	89.69	82.72
H_2O	2.33	2.24	2.62
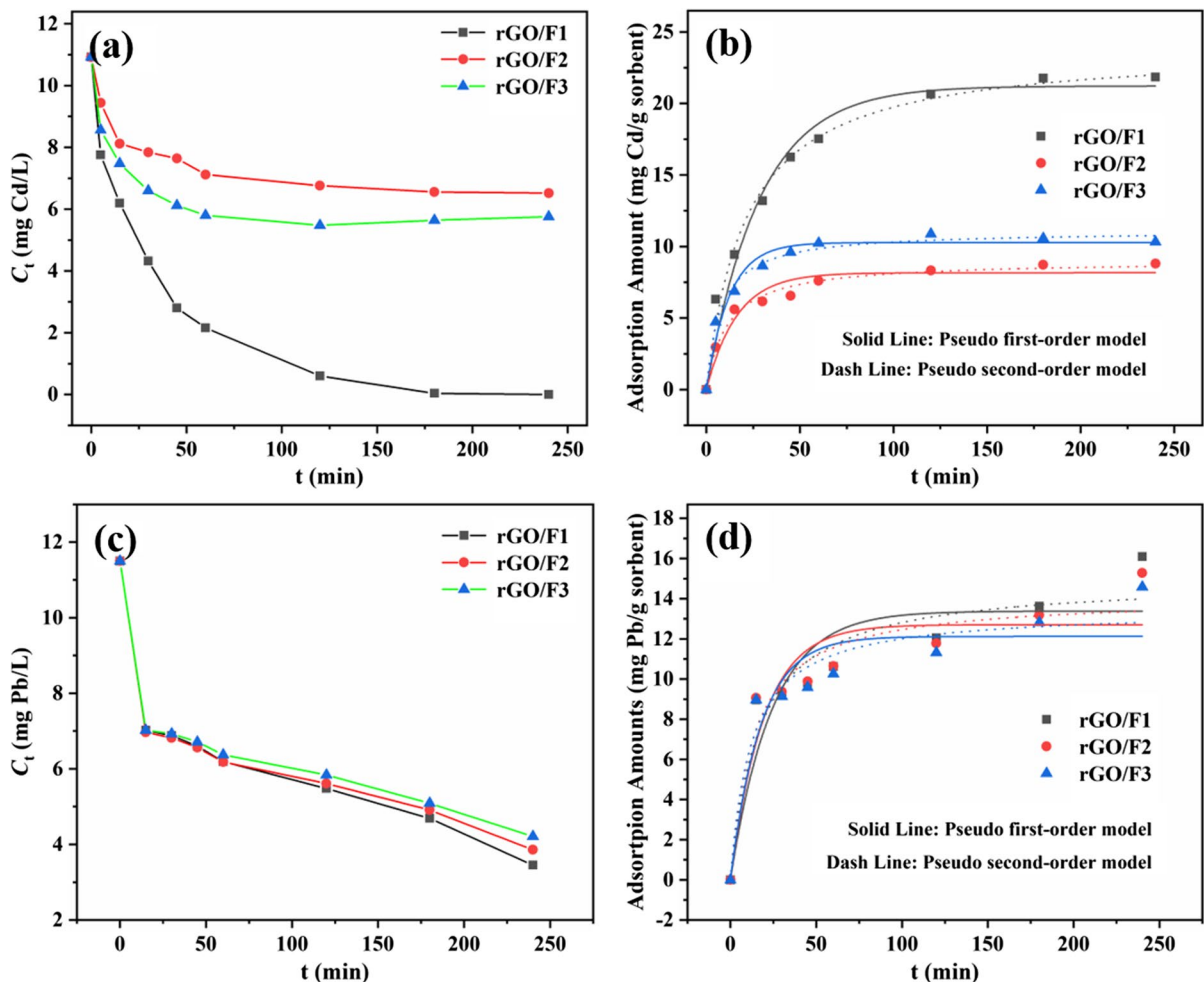
Fig. 10 Adsorption performance of rGO/Fx and PFO/PSO fitting curves: Cd^{2+} (**a**, **b**) and Pb^{2+} (**c**, **d**). ([Cd^{2+}] = 10.92 mg/L, m/V = 0.5 g/L, pH = 4.94, t = 0–240 min; [$Pb.^{2+}$] = 11.5 mg/L, m/V = 0.5 g/L, pH = 5.07, t = 0–240 min)

respectively) compared with those of rGO/F2 (6.56 and 3.86 mg/L for Cd^{2+} and Pb^{2+}, respectively) and rGO/F3 (5.76 and 4.21 mg/L for Cd^{2+} and Pb^{2+}, respectively). As calculated from Eq. 1, the adsorption amount of rGO/F1 (21.84 and 16.10 mg/g for Cd^{2+} and Pb^{2+}, respectively) was higher than those of rGO/F2 (8.80 and 15.28 mg/g for Cd^{2+} and Pb^{2+}, respectively) and rGO/F3 (10.32 and 14.58 mg/g for Cd^{2+} and Pb^{2+}, respectively). The inhibiting effect may be related to the iron oxides or hydroxides, since these products may consume some active sites in the synthesis stage.

The kinetic fitting curves are presented in Fig. 10b and d, and these parameters are listed in Table 3. It is obvious that PSO (R^2 = ~0.9848, ~0.9125) can fit

better than PFO (R^2 = ~0.9391, ~0.8380) both for Cd^{2+} and Pb^{2+} adsorption. This indicated the rate-limiting step in adsorption was chemical adsorption (Chen et al., 2015; Gao et al., 2019; Vijayakumar et al., 2021). (The discussion of the intra-particle diffusion model (Eq. S1 and Fig. S1) can be found in Supplementary Materials). The oxygen-containing groups of GO sheets may serve as predominating active sites for heavy metals elimination (Koilraj et al., 2019). (Table S1 shows the performance of the rGO/Fx and other similar magnetic materials in the literature.)

Moreover, the rGO/Fx can be magnetically retrieved from solution after use. This merit would make them stand out, and would be very helpful for practical application.

Table 3 The parameters calculated from the PFO and PSO models (adsorption of Cd^{2+} and Pb^{2+} by rGO/Fx)

		Pseudo first-order model			Pseudo second-order model		
		q_e (mg/g)	k_1 (min^{-1})	R^2	q_e (mg/g)	k_2 (g mg^{-1} min^{-1})	R^2
Cd(II)	rGO/F1	21.21	0.034	0.9707	23.94	0.002	0.9895
	rGO/F2	8.16	0.061	0.9391	9.01	0.010	0.9848
	rGO/F3	10.27	0.082	0.9676	11.10	0.012	0.9897
Pb(II)	rGO/F1	13.38	0.041	0.8380	14.96	0.004	0.9125
	rGO/F2	12.70	0.052	0.8554	14.12	0.005	0.9262
	rGO/F3	12.12	0.057	0.8536	13.46	0.006	0.9253

4 Conclusions

In this study, a two-step strategy was proposed to prepare a family of magnetic reduced graphene oxide aerogels (abbreviated as rGO/Fx series, x = 1, 2 and 3). Poly(vinyl) alcohol was demonstrated to be essential in maintaining the rGO/Fx morphology. The rGO/Fx showed a unique structure with nanoparticles and nanoplates embedded on rGO sheets. The rGO/Fx consisted of PVA, rGO and Fe-based species (Fe_3O_4, Fe^0 and FeOOH). The specific surface areas were 23.9, 33.6 and 29.1 m^2/g and the saturation magnetizations were 0.50, 0.72 and 9.59 emu/g for rGO/F1, rGO/F2 and rGO/F3, respectively. The impressive magnetic property of rGO/Fx can be tunable by the mass ratio of Fe/GO. The rGO/Fx were able to efficiently remove Cd^{2+} and Pb^{2+} from water. This study may offer a new synthesis method of magnetic aerogels and an effective adsorbent for capturing heavy metals from water.

Authors Contribution   Jiang-Bo Huo: Conceptualization, Methodology, Validation, Writing- original draft. Guoce Yu: Conceptualization, Writing—review & editing, Project administration, Funding acquisition.

Data Availability   All data generated or analyzed during this study are included in this published article (and its supplementary information files).

Declarations

Competing Interest   The authors declare that they have no known competing financial interests or personal relationships that could have appeared to influence the work reported in this paper.

References

Arabkhani, P., & Asfaram, A. (2020). Development of a novel three-dimensional magnetic polymer aerogel as an efficient adsorbent for malachite green removal. *Journal of Hazardous Materials, 384*, 121394.

Cao, X., Yin, Z., & Zhang, H. (2014). Three-dimensional graphene materials: Preparation, structures and application in supercapacitors. *Energy & Environmental Science, 7*(6), 1850–1865.

Chen, H., Gao, B., & Li, H. (2015). Removal of sulfamethoxazole and ciprofloxacin from aqueous solutions by graphene oxide. *Journal of Hazardous Materials, 282*, 201–207.

Chen, W., & Yan, L. (2011). In situ self-assembly of mild chemical reduction graphene for three-dimensional architectures. *Nanoscale, 3*(8), 3132–3137.

Chen, Y.-P., Yang, L.-M., Paul Chen, J., & Zheng, Y.-M. (2019). Electrospun spongy zero-valent iron as excellent electro-Fenton catalyst for enhanced sulfathiazole removal by a combination of adsorption and electro-catalytic oxidation. *Journal of Hazardous Materials, 371*, 576–585.

Cong, H.-P., Chen, J.-F., & Yu, S.-H. (2014). Graphene-based macroscopic assemblies and architectures: An emerging material system. *Chemical Society Reviews, 43*(21), 7295–7325.

Cong, H. P., Ren, X. C., Wang, P., & Yu, S. H. (2012). Macroscopic multifunctional graphene-based hydrogels and aerogels by a metal ion induced self-assembly process. *ACS Nano, 6*(3), 2693–2703.

Dai, H., Huang, Y., & Huang, H. (2018). Eco-friendly polyvinyl alcohol/carboxymethyl cellulose hydrogels reinforced with graphene oxide and bentonite for enhanced adsorption of methylene blue. *Carbohydrate Polymers, 185*, 1–11.

Dai, S., Wang, N., Qi, C., Wang, X., Ma, Y., Yang, L., Liu, X., Huang, Q., Nie, C., Hu, B., & Wang, X. (2019). Preparation of core-shell structure Fe_3O_4@C@MnO_2 nanoparticles for efficient elimination of U(VI) and Eu(III) ions. *Science of the Total Environment, 685*, 986–996.

De Silva, K. K. H., Huang, H. H., Joshi, R. K., & Yoshimura, M. (2017). Chemical reduction of graphene oxide using green reductants. *Carbon, 119*, 190–199.

Feng, Y., Zhang, H., Xin, B., & Wu, J. (2017). Magnetically recyclable reduced graphene oxide nanosheets/magnetite-palladium aerogel with superior catalytic activity and

reusability. *Journal of Colloid and Interface Science, 506*, 154–161.

Fu, G., Yan, X., Chen, Y., Xu, L., Sun, D., Lee, J. M., & Tang, Y. (2018). Boosting bifunctional oxygen electrocatalysis with 3D graphene aerogel-supported Ni/MnO particles. *Advanced Materials, 30*(5), 1704609.

Gao, Y., Kang, R., Xia, J., Yu, G., & Deng, S. (2019). Understanding the adsorption of sulfonamide antibiotics on MIL-53s: Metal dependence of breathing effect and adsorptive performance in aqueous solution. *Journal of Colloid and Interface Science, 535*, 159–168.

Guo, X., & Wang, J. (2019). A general kinetic model for adsorption: Theoretical analysis and modeling. *Journal of Molecular Liquids, 288*, 111100.

Jiang, L., & Fan, Z. (2014). Design of advanced porous graphene materials: From graphene nanomesh to 3D architectures. *Nanoscale, 6*(4), 1922–1945.

Kemp, K. C., Seema, H., Saleh, M., Le, N. H., Mahesh, K., Chandra, V., & Kim, K. S. (2013). Environmental applications using graphene composites: Water remediation and gas adsorption. *Nanoscale, 5*(8), 3149–3171.

Koilraj, P., Kalusulingam, R., & Sasaki, K. (2019). Arginine and lysine-functionalized layered double hydroxides as efficient sorbents for radioactive Co2+ removal by chelate-facilitated immobilization. *Chemical Engineering Journal, 374*, 359–369.

Li, Y., Li, L., Chen, T., Duan, T., Yao, W., Zheng, K., Dai, L., & Zhu, W. (2018a). Bioassembly of fungal hypha/graphene oxide aerogel as high performance adsorbents for U(VI) removal. *Chemical Engineering Journal, 347*, 407–414.

Li, Z., Wang, L., Meng, J., Liu, X., Xu, J., Wang, F., & Brookes, P. (2018b). Zeolite-supported nanoscale zero-valent iron: New findings on simultaneous adsorption of Cd(II), Pb(II), and As(III) in aqueous solution and soil. *Journal of Hazardous Materials, 344*, 1–11.

Liang, Q., Luo, H., Geng, J., & Chen, J. (2018). Facile one-pot preparation of nitrogen-doped ultra-light graphene oxide aerogel and its prominent adsorption performance of Cr(VI). *Chemical Engineering Journal, 338*, 62–71.

Luo, B., & Zhi, L. (2015). Design and construction of three dimensional graphene- based composites for lithium ion battery applications. *Energy & Environmental Science, 8*(2), 456–477.

Mao, J., Iocozzia, J., Huang, J., Meng, K., Lai, Y., & Lin, Z. (2018). Graphene aerogels for efficient energy storage and conversion. *Energy & Environmental Science, 11*(4), 772–799.

Mao, S., Lu, G., & Chen, J. (2015). Three-dimensional graphene-based composites for energy applications. *Nanoscale, 7*(16), 6924–6943.

Mohammadian, M., Sahraei, R., & Ghaemy, M. (2019). Synthesis and fabrication of antibacterial hydrogel beads based on modified-gum tragacanth/poly(vinyl alcohol)/Ag(0) highly efficient sorbent for hard water softening. *Chemosphere, 225*, 259–269.

Perreault, F., de Faria, A. F., & Elimelech, M. (2015). Environmental applications of graphene-based nanomaterials. *Chemical Society Reviews, 44*(16), 5861–5896.

Qiu, B., Xing, M., & Zhang, J. (2018). Recent advances in three-dimensional graphene based materials for catalysis applications. *Chemical Society Reviews, 47*(6), 2165–2216.

Sahraei, R., Sekhavat Pour, Z., & Ghaemy, M. (2017). Novel magnetic bio-sorbent hydrogel beads based on modified gum tragacanth/graphene oxide: Removal of heavy metals and dyes from water. *Journal of Cleaner Production, 142*, 2973–2984.

Shao, J., Feng, J., Zhou, H., & Yuan, A. (2019). Graphene aerogel encapsulated Fe-Co oxide nanocubes derived from Prussian blue analogue as integrated anode with enhanced Li-ion storage properties. *Applied Surface Science, 471*, 745–752.

Shen, Y., Fang, Q., & Chen, B. (2015). Environmental applications of three-dimensional graphene-based macrostructures: Adsorption, transformation, and detection. *Environmental Science & Technology, 49*(1), 67–84.

Tang, J., & Wang, J. (2018a). Fenton-like degradation of sulfamethoxazole using Fe-based magnetic nanoparticles embedded into mesoporous carbon hybrid as an efficient catalyst. *Chemical Engineering Journal, 351*, 1085–1094.

Tang, J., & Wang, J. (2018b). Metal organic framework with coordinatively unsaturated sites as efficient fenton-like catalyst for enhanced degradation of sulfamethazine. *Environmental Science & Technology, 52*(9), 5367–5377.

Tang, J., & Wang, J. (2019). MOF-derived three-dimensional flower-like FeCu@C composite as an efficient Fenton-like catalyst for sulfamethazine degradation. *Chemical Engineering Journal, 375*, 122007.

Upadhyay, R. K., Soin, N., & Roy, S. S. (2014). Role of graphene/metal oxide composites as photocatalysts, adsorbents and disinfectants in water treatment: A review. *RSC Advances, 4*(8), 3823–3851.

Vafakhah, S., Guo, L., Sriramulu, D., Huang, S., Saeedikhani, M., & Yang, H. Y. (2019). Efficient sodium-ion intercalation into the freestanding prussian blue/graphene aerogel anode in a hybrid capacitive deionization system. *ACS Applied Materials & Interfaces, 11*(6), 5989–5998.

Vijayakumar, E., Govinda Raj, M., Neppolian, B., Kumar Lakhera, S., & John Bosco, A. (2021). Hierarchical layered nanostructure of MoS$_2$/boron doped reduced graphene oxide composites under visible light irradiation for effective antibiotic degradation and hexavalent chromium reduction. *Materials Letters, 296,* 129891.

Wu, Z., Deng, W., Zhou, W., & Luo, J. (2019). Novel magnetic polysaccharide/graphene oxide@Fe$_3$O$_4$ gel beads for adsorbing heavy metal ions. *Carbohydrate Polymers, 216*, 119–128.

Xia, W., Qu, C., Liang, Z., Zhao, B., Dai, S., Qiu, B., Jiao, Y., Zhang, Q., Huang, X., Guo, W., Dang, D., Zou, R., Xia, D., Xu, Q., & Liu, M. (2017). High-performance energy storage and conversion materials derived from a single metal-organic framework/graphene aerogel composite. *Nano Letters, 17*(5), 2788–2795.

Xiao, L., Wu, D., Han, S., Huang, Y., Li, S., He, M., Zhang, F., & Feng, X. (2013). Self-assembled Fe(2)O(3)/graphene aerogel with high lithium storage performance. *ACS Applied Materials & Interfaces, 5*(9), 3764–3769.

Xu, Y. X., Sheng, K. X., Li, C., & Shi, G. Q. (2010a). Self-assembled graphene hydrogel via a one-step hydrothermal process. *ACS Nano, 4*(7), 4324–4330.

Xu, Y. X., Wu, Q. O., Sun, Y. Q., Bai, H., & Shi, G. Q. (2010b). Three-dimensional self-assembly of graphene oxide and DNA into multifunctional hydrogels. *ACS Nano, 4*(12), 7358–7362.

Yao, T., Jia, W., Feng, Y., Zhang, J., Lian, Y., Wu, J., & Zhang, X. (2019a). Preparation of reduced graphene oxide nanosheet/FexOy/nitrogen-doped carbon layer aerogel as photo-Fenton catalyst with enhanced degradation activity and reusability. *Journal of Hazardous Materials, 362*, 62–71.

Yao, T., Qi, Y., Mei, Y., Yang, Y., Aleisa, R., Tong, X., & Wu, J. (2019b). One-step preparation of reduced graphene oxide aerogel loaded with mesoporous copper ferrite nanocubes: A highly efficient catalyst in microwave-assisted Fenton reaction. *Journal of Hazardous Materials, 378*, 120712.

Yi, X., Sun, F., Han, Z., Han, F., He, J., Ou, M., Gu, J., & Xu, X. (2018). Graphene oxide encapsulated polyvinyl alcohol/sodium alginate hydrogel microspheres for Cu (II) and U (VI) removal. *Ecotoxicology and Environmental Safety, 158*, 309–318.

Yu, R., Shi, Y., Yang, D., Liu, Y., Qu, J., & Yu, Z. Z. (2017). Graphene oxide/chitosan aerogel microspheres with honeycomb-cobweb and radially oriented microchannel structures for broad-spectrum and rapid adsorption of water contaminants. *ACS Applied Materials & Interfaces, 9*(26), 21809–21819.

Zakaria, Z., & Kamarudin, S. K. (2021). Effect of alkali doping on alkaline stability and cell performance of quaternization polyvinyl alcohol/graphene oxide membranes for passive DEFCs. *Materials Letter, 292,* 129651.

Zhang, W., Deng, Q., He, Q., Song, J., Zhang, S., Wang, H., Zhou, J., & Zhang, H. (2018). A facile synthesis of core-shell/bead-like poly (vinyl alcohol)/alginate@PAM with good adsorption capacity, high adaptability and stability towards Cu(II) removal. *Chemical Engineering Journal, 351*, 462–472.

Zhuang, Y., Wang, X., Zhang, L., Dionysiou, D. D., & Shi, B. (2019). Fe-Chelated polymer templated graphene aerogel with enhanced Fenton-like efficiency for water treatment. *Environmental Science: Nano, 6*(11), 3232–3241.

Zou, Y., Wang, X., Khan, A., Wang, P., Liu, Y., Alsaedi, A., Hayat, T., & Wang, X. (2016). Environmental remediation and application of nanoscale zero-valent iron and its composites for the removal of heavy metal ions: A review. *Environmental Science & Technology, 50*(14), 7290–7304.